Mon. Not. R. astr. Soc. (1988) **233,** 649–666

Consequences of a chromospheric temperature rise on the formation of the Hα line in late-type supergiants

Sushma V. Mallik and D. C. V. Mallik *Indian Institute of Astrophysics, Bangalore 560034, India*

Accepted 1988 February 8. Received 1988 January 26; in original form 1987 October 21

Summary. New radiative transfer calculations of Hα in differentially expanding non-isothermal spherical chromospheres have been performed, including explicitly the effect of hydrogen ionization. The source function for Hα and the emergent line profile have been computed for a variety of temperature structures, densities, chromospheric extents and velocity gradients in order to explore sensitivity of the Hα line to these various properties of the chromosphere. The observed characteristics of the line in a sample of G and K supergiants have been matched with the theoretical profiles to obtain densities, expansion velocities and extents of the Hα forming regions of these stars. While the temperature structures used here are schematic, they provide sensitive constraints on the appearance of the Hα line in these types of stars. From a comparison of the observed profiles with the computed ones, we obtain total hydrogen densities in the range 10^9–10^{11} cm^{-3} at the base of the line forming region, integrated chromospheric optical depths in Hα in the range 50–5000, and expansion velocities in the range 0.25–2 times the maximum random (microturbulent and thermal) velocity. The inferred mass loss rates turn out to be in the range 10^{-7} to 10^{-9} $M_\odot$ yr^{-1}. Our calculations do not satisfactorily explain the blue emission observed in several stars.

1 Introduction

Most K and M giants and G, K and M supergiants lose mass in the form of cool stellar winds (Reimers 1981; Linsky 1985; Dupree 1986). An important diagnostic of mass outflow in these stars is the absorption component of a line at negative radial velocity. The Hα profile at 6563 Å in late G and K supergiants is a strong absorption feature with a distinct blue asymmetry characteristic of outflowing atmospheres (Mallik 1979; Zarro & Rodgers 1983). Small emission components are often seen on the blue or the red or both sides of the absorption profile. Being in the red region of the spectrum, the Hα line is easily observable in a large number of these stars at high dispersion. Despite these advantages, only a few studies have focused on this line as a potential optical signature of mass loss (Boesgaard & Hagen 1979; Mallik 1979; Dupree, Hartmann &

Avrett 1984a; Dupree *et al.* 1984b). Being a subordinate photoionization controlled line, its description depends crucially upon the mechanism of excitation of the hydrogen levels and requires a detailed knowledge of the local temperature and density conditions and of the local radiation field for line and continuum processes. Further, since the line is principally of chromospheric origin and the chromospheres of the stars under consideration are extended and expanding (Goldberg *et al.* 1982; Hartmann 1983; Drake & Linsky 1986), a spherically symmetric moving atmospheres technique has to be used for describing the Hα transfer. Several attempts have been made in the past to model usually the resonance lines (Mg II *h* and *k*, Ca II *H* and *K*) in the chromospheres, almost all of them restricted to plane-parallel, static atmospheres (Kelch, Linsky & Worden 1979; Ayres & Linsky 1975; Baliunas *et al.* 1979; Basri, Linsky & Ericksson 1981). Recently, Drake & Linsky (1983) have developed a non-LTE computer code using the comoving frame formulation of Mihalas, Kunasz & Hummer (1975) and Mihalas *et al.* (1976) and used the same to infer mass loss rates of cool stars by matching the observed asymmetric emission lines of Mg II. Based on the theory of Alfvén-wave driven winds (Hartmann & MacGregor 1980), Hartmann & Avrett (1984) have also made spherically symmetric calculations for a variety of diagnostics including Hα in an expanding model chromosphere of α Ori (M2Iab) to match the extended distribution of emission inferred from spectral imaging and radio observations.

Being primarily collision-dominated, the Ca II *H* and *K* and Mg II *h* and *k* have been the standard diagnostics of the local conditions, e.g. temperatures and densities of the chromospheres. On the other hand, the Hα source function and the absorption profile were believed to provide no sensitive constraints on the chromospheric densities and temperatures (Gebbie & Steinitz 1974). However, a close look at the line source function has shown this to be incorrect. The scattering integral depends upon the absorption profile and the intensity field, which carry respectively information on the temperature and density (Cram & Mullan 1985).

Since in reality, the chromosphere has a temperature rise across it, there is a corresponding increase in the thermal Doppler width which affects the absorption width of Hα, as it has a substantial thermal Doppler contribution. The $n=2$ level population is similarly controlled by the temperature–density structure through excitation and ionization. Zarro (1984) has demonstrated in a schematic analytic calculation that the Hα optical depth and, in turn, the absorption width are actually coupled to the thermal structure particularly if the temperature rise is steep. Dupree *et al.* (1984a, b) have analysed the appearance of the Hα line in Population II giants with the help of static and expanding chromospheric models. The observed strong asymmetric emission in the wings with asymmetric absorption cores could be explained with expanding spherical chromospheres having a temperature distribution with a steep rise followed by a wide plateau of several stellar radii at 8000–10 000 K. The computed Hα profiles were found to be very sensitive to the temperature structure. In an earlier work (Mallik 1986), detailed Hα transfer calculations were performed and line profiles were computed, for a wide variety of parameters in order to cover the observed characteristics of 23 G and K supergiants. Although this work was based on a non-LTE approach to the transfer problem, the calculations were restricted to isothermal chromospheres; the hydrogen ionization was not taken into account either. The present work is undertaken to investigate the consequences of temperature gradients and ionization on the Hα line profile. We have explored in detail the sensitivity of the Hα source function and the emergent line profile to temperature structure, chromospheric extent, densities and velocity gradients. We have used schematic but reasonable temperature structures already available in the literature for stars of the kind we are discussing here. As we shall see, the inclusion of the thermal structure changes the appearance of the profiles rather drastically and also modifies the interpretation of optical depths, initial densities and mass outflow rates. In Section 2 we discuss the theory of the Hα transfer including the above effects. The computation of the line profiles and their analysis and interpretation are described in Section 3 followed by the conclusions in Section 4.

2 Theory

We model the chromosphere as a non-LTE, spherical expanding atmosphere with given velocity, density and temperature distributions. We use the comoving frame technique of radiative transfer developed by Peraiah (1980a, b, 1981). (For details see Mallik 1986.) Hartmann & Avrett (1984) made *ab initio* calculations of the chromosphere of α Ori (M2Iab). They adjusted the temperature structure of the atmosphere until the calculated radiative losses balanced the heating rate as expected from Alfvén wave dissipation. Although their method of computing density, temperature and velocity structures is internally self-consistent, there exist discrepancies with observed fluxes and line shapes.

We have adopted a schematic approach in which the model chromosphere is divided into a discrete number of shells with the inner point near the region of temperature minimum, assumed to be the stellar radius, R_*. We assume that the radiation incident on R_* is the stellar photospheric continuum from below, characterized by a Planck function $B(T_R)$ of radiation temperature T_R as defined in Hartmann & MacGregor (1980). The other boundary conditions of our problem are that the radiation incident on the outer radius R_{max} from outside is zero and the frequency derivative of the specific intensity $\partial I/\partial x=0$ at the two end-points of the frequency grid chosen in the comoving frame calculations.

Following the schematic description of the temperature rise in the chromosphere in earlier works (Dupree *et al.* 1984a, b; Cram & Mullan 1985; Dupree 1986), we have tried various plausible temperature structures. As pointed out by Cram & Mullan (1985), these are not based on either quantitative observations or explicit theoretical studies of the chromospheric energy balance. Nevertheless the assumed outward rise of the *ad hoc* temperature distributions does reflect the consequence of non-radiative chromospheric heating. The calculations with these schematic temperature structures are mainly of an exploratory nature. Since in the transfer code that we use, the depth dependence of the input parameters is expressed in terms of the radial coordinate r, we have tried to describe the temperature distribution also in a similar fashion instead of the conventional way of expressing it in terms of the mass density. To start with, a linear rise of T with $\log r$ was adopted, very similar to the structure assumed by Cram & Mullan (1985).

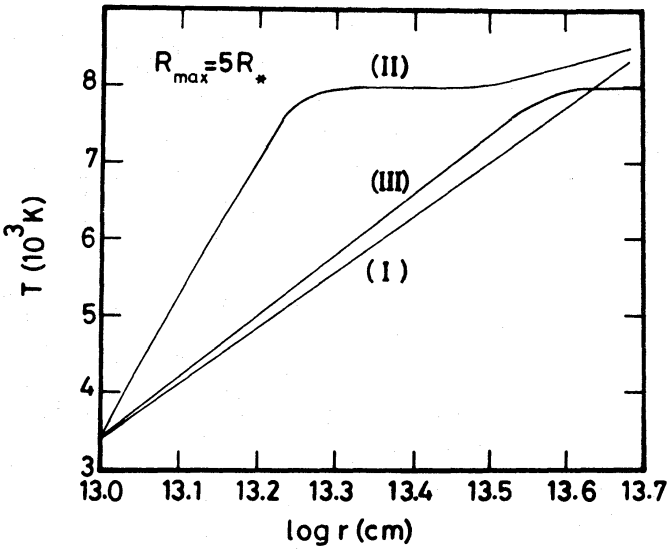

Figure 1. The temperature distribution as a function of the radial distance r (cm) characterized by T_I; a linear climb in $\log r$ from T_* (~3400 K for a star of effective temperature 4250 K) at R_* to 8000 K at the outer radius R_{max}, T_{II}: a steep climb to 8000 K well inside of R_{max} followed by a broad plateau over the rest of the line forming extent and T_{III}: a linear climb in $\log r$ with a plateau in the last few shells. These refer to the particular case of $R_{max}=5R_*$.

The second distribution that we have used, roughly follows the one used by Dupree *et al.* (1984a, b). In this there is a steep linear climb in T versus $\log r$ from the temperature minimum T_* to ~8000 K within a short distance from the photosphere followed by a broad plateau extending over several R_*s. Drake (1985) had assumed a similar structure in his attempt to reproduce the Mg II emission in α Boo. A third distribution attempted by us is a linear T climb with $\log r$ almost all the way through the line-forming region and then a plateau in the very outer layers. Fig. 1 displays the three typical temperature distributions used in our model. There is no *a priori* justification for using these schematic structures other than what has already been said above. The sensitivity of the computed profiles to these schemes will constrain the choice of temperature gradients and chromospheric extents.

The nature of the blue asymmetry commonly observed in Hα implies that the velocity is increasing outward (Hummer & Rybicki 1968). We have assumed a linear gradient in velocity with $V(r)=V_{\max}$ at $R_{\max}$. Assuming a mass conservative flow, the density then is $\propto r^{-3}$. We further assume that for the temperature range prevalent in the G and K supergiants (3500–8500 K), the Lyman lines and the continua are in radiative detailed balance. Non-LTE calculations even in low density models of α Ori (Hartmann & Avrett 1984) suggest that this approximation holds for Hα.

We have used the formulation of Vernazza, Avrett & Loeser (1973) suitably modified for a two-level atom with continuum to describe the $n=2$ level population. We assume that the population in a given level is determined by the balance between photoionization from the level due to the stellar photospheric continuum and direct radiative recombination. Then, we can write

$$n_1=n_e n_p b_1 \psi(T),$$

where

$$\psi(T)=\left(\frac{h^2}{2\pi m_e kT}\right)^{3/2} \exp\left(\frac{I_1}{kT}\right),$$

and

$$n_2=4n_1 \exp(-h\nu_{12}/kT)=4n_e n_p b_1 \psi(T) \exp(-h\nu_{12}/kT).$$

We assume a pure hydrogen atmosphere, i.e. $n_e=n_p$. It is also assumed that the total hydrogen density n_H is given by $n_H=n_1+n_p$.

Given n_H, T, T_R and b_1, n_p and hence n_2 can be calculated. Hartmann & MacGregor (1980) used the same arguments to derive the electron densities and cooling rates in cool chromospheres. We use their general expression for b_1 for a star of effective temperature ~4250 K, which is

$$b_1=\frac{T}{WT_R} \exp\left[\frac{I_1}{k}\left(\frac{1}{4T_R}+\frac{3}{4T_1}-\frac{1}{T}\right)\right],$$

where for $T<6000$: $T_R=3800$, $T_1=T$; for $6000\leq T\leq 8000$: $T_R=3800+1.6(T-6000)$, $T_1=6000+0.5(T-6000)$; for $T>8000$; $T_R=T_1=7000$. T_R is the radiation temperature representing the continuum radiation field causing the photoionization.

One of the important consequences of the T and n_H structures and the inclusion of ionization is the depth dependence of n_2 which is very different from the isothermal case. n_2 does not follow the outward fall in n_H, the temperature rise more than compensating for the fall in n_H. It actually goes up steadily until a high enough temperature (depending upon density) is reached when the ionization from the $n=2$ level becomes important and n_2 starts declining. n_2 directly affects the run of optical depth in the line-forming region which in turn determines the structure of the Hα profile. In the model of Hartmann & Avrett (1984), n_2 after an initial rise drops by several orders

of magnitude over the chromospheric extent, commensurate with a similar drop in n_H. Hebden, Eckart & Hege (1987) obtain an intensity profile of Hα by speckle imaging matching closely the one calculated by Hartmann & Avrett (1984). In our model, the drop in n_H is 1 or 2 orders of magnitude. n_2 reflects a similar structure.

A more subtle effect is produced by the depth variation of the profile function. Assuming it to be Gaussian, we write for the profile $\phi(x,\delta)=1/\delta\sqrt{\pi}\exp(-x^2/\delta^2)$ where $\delta=\Delta\nu_D(r)/\Delta\nu_D^{ref}$ and choose $\Delta\nu_D^{ref}$ to be the value at R_{max}. A microturbulent term is also included in $\Delta\nu_D$. The Doppler width is thus smallest at R_* and largest at R_{max}. Due to progressive widening of the profile function, radiation from deeper layers at frequencies far from the line centre, which would escape unimpeded in the isothermal case, now suffers effects of transfer with increasing scattering in the wings. At the upper layers, radiation far out in the wings escapes after relatively few scatterings.

The source function in our program is given by

$$S(x,\ r)=\frac{\phi(x,\ r)}{\beta+\phi(x,\ r)}\,S_l(r)+\frac{\beta}{\beta+\phi(x,\ r)}\,S_c(r),$$

where β is the ratio of the continuum opacity to the line opacity, S_c is the continuum source function set equal to $B(T_R)$, the Planck function of radiation temperature T_R which also defines the stellar photospheric continuum. $S_l(r)$, the line source function, is

$$S_l(r)=\int_{-\infty}^{\infty}\phi(x',\ r')\,dx'\int_{-1}^{1}I(x',\ \mu',\ r')\,d\mu'+\varepsilon B(r),$$

where ε is the photon destruction probability by collisional de-excitation and $B(r)$ the Planck function characterized by the temperature $T(r)$. The above expression for $S_l(r)$ tacitly assumes the usual complete redistribution (CRD) for emitted and absorbed photons which is a good approximation for non-resonance lines such as Hα. We have calculated representative values of ε and β for the density and temperature ranges that we have chosen. T_R is assumed from the formula given by Hartmann & MacGregor (1980).

With $T(r)$, $T_R(r)$, $V(r)$, $n_H(r)$, $\phi(r)$ as inputs into the transfer code, the Hα source functions have been computed and the emergent line profiles calculated after a transformation into the observer's frame. Since the number of free parameters is large and a wide range in each is possible, it is difficult to deconvolve the information on the atmospheric structure uniquely from one observed line profile. Nevertheless, it is worth exploring the sensitivity of the line profiles to input parameters like the maximum outflow velocity, the outer radius of the expanding envelope, the temperature gradient of the chromosphere, the total hydrogen density at R_*, and the consequent integrated line centre optical depth τ. The choice of the range of the above parameters is dictated by the following considerations based on the observed physical properties of the chromospheres of G–M supergiants:

(i) The microturbulence deduced from the chromospheric lines is quite large – of the order 5–25 km s^{-1} (Kuhi 1974; Hartmann, Dupree & Raymond 1981; Ayres *et al.* 1982; Hartmann 1983). It is possible that microturbulence increases through the chromosphere (Jordan & Linsky 1987), but we have not considered this variation in the present work. We have adopted a constant value of 15 km s^{-1}. The random velocity (thermal+microturbulent) V_{Dopp} at R_{max} then amounts to ~20 km s^{-1} for the temperature chosen there. $\Delta\nu_D^{ref}$ is the reference Doppler width corresponding to the maximum random velocity, i.e. V_{Dopp} at R_{max}.

(ii) The winds have low velocities with the maximum outflow velocity V_{max} only 0.5–3 times the maximum random velocity.

(iii) The chromospheres extend out to at least a few stellar radii. Radio continuum emission observations of cool giants and supergiants (Drake & Linsky 1986) and speckle interferometry

and imaging of Hα of α Ori (Goldberg *et al.* 1982; Hebden *et al.* 1987) all suggest extended chromospheres.

For the purpose of our calculations, R_{max} up to $6R_*$, V_{max} up to $4V_{Dopp}$, τ up to a few times 10^4 and a variety of temperature structures have been tried in order to cover the range of observed Hα characteristics in the sample of G and K supergiants which have already been described by Mallik (1982).

3 Analysis and interpretation of the line profiles

3.1 SENSITIVITY OF LINE PROFILES TO INPUT PARAMETERS

As mentioned in the previous section, we have tried three plausible temperature structures (Fig. 1) which have been used earlier by other authors to reproduce observed chromospheric line profiles. We identify these as follows:

I. Linear increase of T with $\log r$: $T_I(r)$
II. Steep climb of T to 8000 K followed by a broad plateau: $T_{II}(r)$
III. Linear increase of T with $\log r$ followed by a narrow plateau at 8000 K: $T_{III}(r)$.

3.1.1 Effect of $T_I(r)$

Fig. 2(a) shows how n_2 varies with r for two extents $R_{max}=5R_*$ and $8R_*$ and for a variety of optical depths. The first few shells close to R_* hardly contribute to Hα because of the low temperatures even though n_H is high. Although n_H is dropping off as r^{-3}, n_2 maintains a high steady value in the rest of the region because of high temperatures. This region therefore contributes more or less evenly to the Hα formation with a peak around ~7000 K beyond which ionization effects come into play and cause a slight decline in n_2. With a higher n_H^0, ionization sets in at a higher

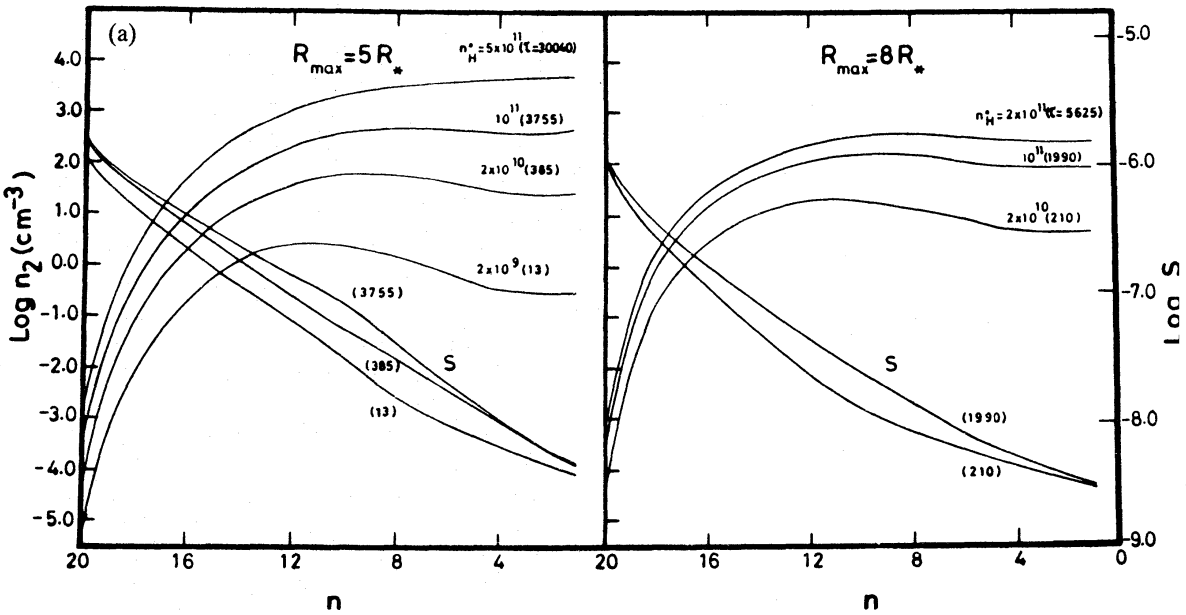

Figure 2. The depth-variation of the $n=2$ population for the three temperature distributions described in Fig. 1 for various extents and densities. n_H^0 refers to the total hydrogen density chosen at R_*, τ is the corresponding integrated optical depth. The shell number $n=20$ refers to the innermost shell at R_* and $n=1$ to the outermost shell at R_{max}. Also shown are the corresponding source functions.

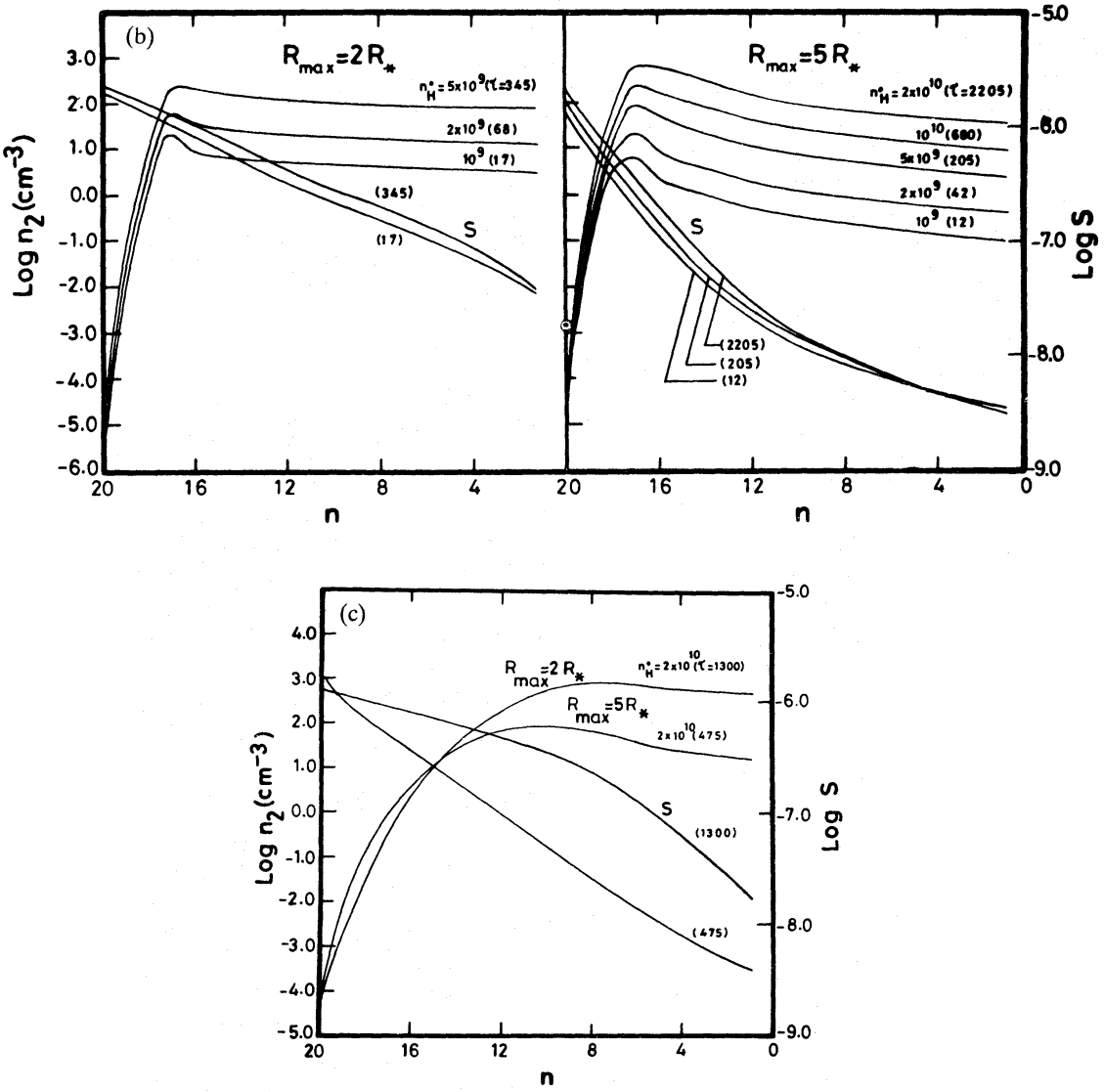

Figure 2–*continued*

temperature, hence a little farther out. For $n_H^0=5\times10^{11}$ cm^{-3}, ionization does not occur at all and n_2 continues to increase.

The source functions in this case (shown in Fig. 2a) are found to decrease by almost three orders of magnitude (between 300 and 1000) over the line-forming region. The basic feature of the computed line is a deep absorption whose strength systematically increases with the assumed initial n_H. A remarkable property of these profiles is that the cores are not saturated as in the isothermal situation even for $\tau>1000$, thus they resemble the observed profiles more closely. Whether this can be attributed to the varying distribution of optical depth or the varying Doppler profile function or both is difficult to conclude as the above two effects of the temperature gradient were not separately studied. Another very important consequence of the temperature gradient is the presence of symmetric blue and red emission flanking the dark absorption for the static case ($V_{max}=0$) even in a pure scattering medium ($\varepsilon=0$). In the previous calculations with isothermal chromospheres and a pure scattering medium (Mallik 1986) no emission was present above the level of continuum for the static case. The symmetry of the emission components disappears as soon as chromospheric expansion is introduced. The expansion causes a blueshift of

the absorption core which covers up most of the emission on the blue side. The overall appearance is that of an asymmetric line characterized by a blueshifted core and brighter red emission. Fig. 3(a) shows a few representative profiles for $T_I(r)$. In this and all the subsequent figures, the velocities on the abscissa are plotted in the sense of being progressively bluer to the right. As has been already found by Drake & Linsky (1983) for the Mg II k line, for a given temperature distribution, profiles respond differently to different chromospheric extents and we discuss this below.

3.1.1.1 $R_{max}/R_*=2$. For this extent, the absorption cores are beautifully rounded with no saturation at all, and very similar in appearance to the observed Hα cores. The blue emission persists at $V_{max}=-10\,km\,s^{-1}$ ($\simeq 0.5\,V_{Dopp}$) and the red emission steadily increases with increasing V_{max}. At $V_{max}=-20\,km\,s^{-1}$ blue emission is absent. The computations were performed for τ as

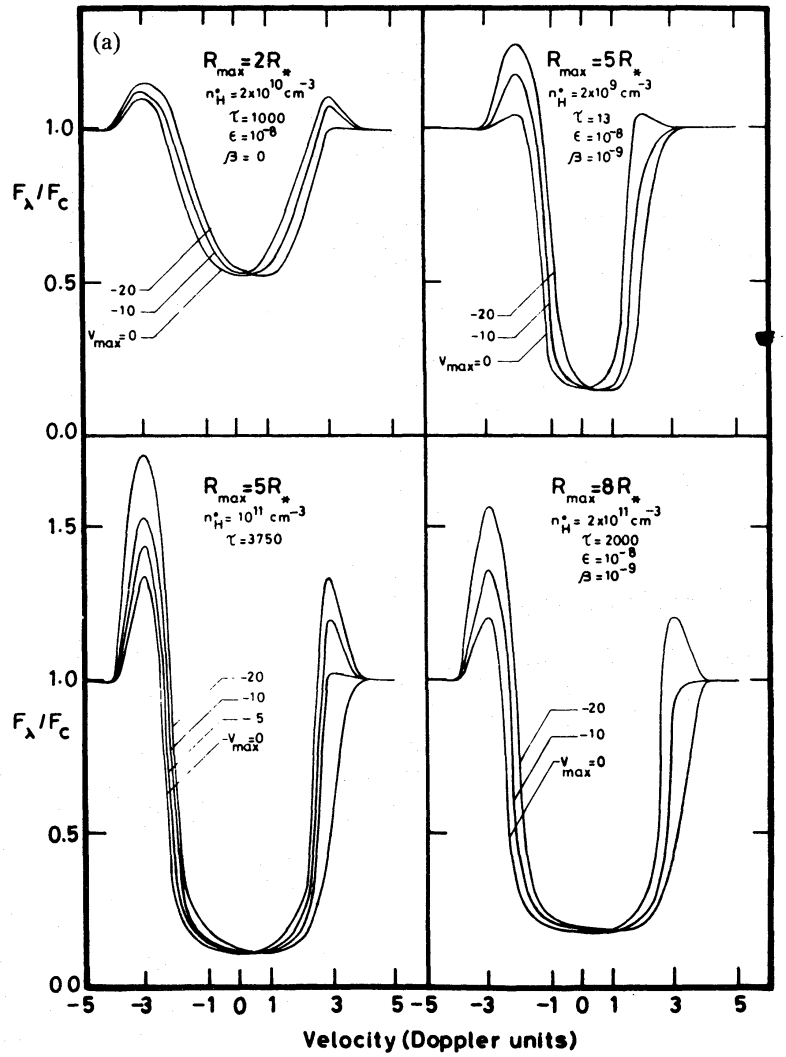

Figure 3. (a) Hα profiles computed for the temperature distribution $T_I(r)$ for a range of densities. R_{max} is specified for each set of profiles. Each profile is denoted by V_{max}, the value of the outflow velocity at R_{max}. The abscissa is expressed in terms of velocity in Doppler units V_{Dopp} referred to at R_{max}, namely $-20\,km\,s^{-1}$. The values on the abscissa in this and all the subsequent figures are plotted in the sense of wavelength decreasing to the right. (b) Hα profiles computed for the temperature distribution $T_{II}(r)$ for $R_{max}=2R_*$ and $5R_*$ with different assumed densities. (c) Computed Hα profiles for the temperature distribution $T_{III}(r)$ for $R_{max}=2R_*$ and $5R_*$. The densities assumed are shown for each set of profiles.

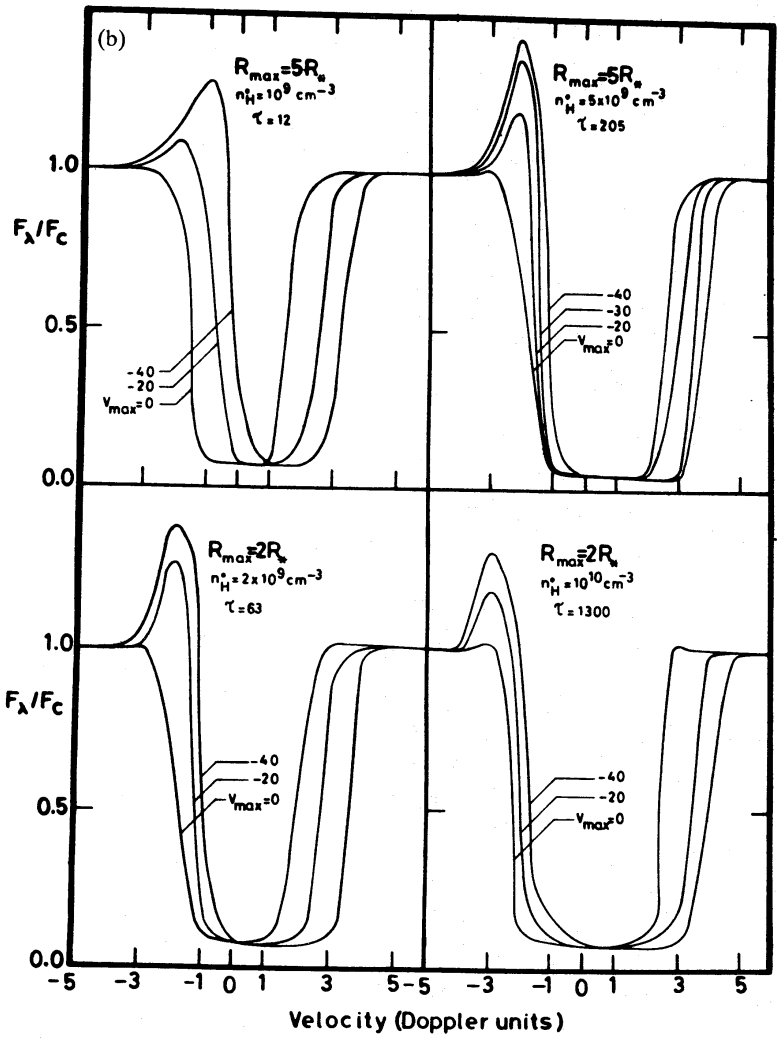

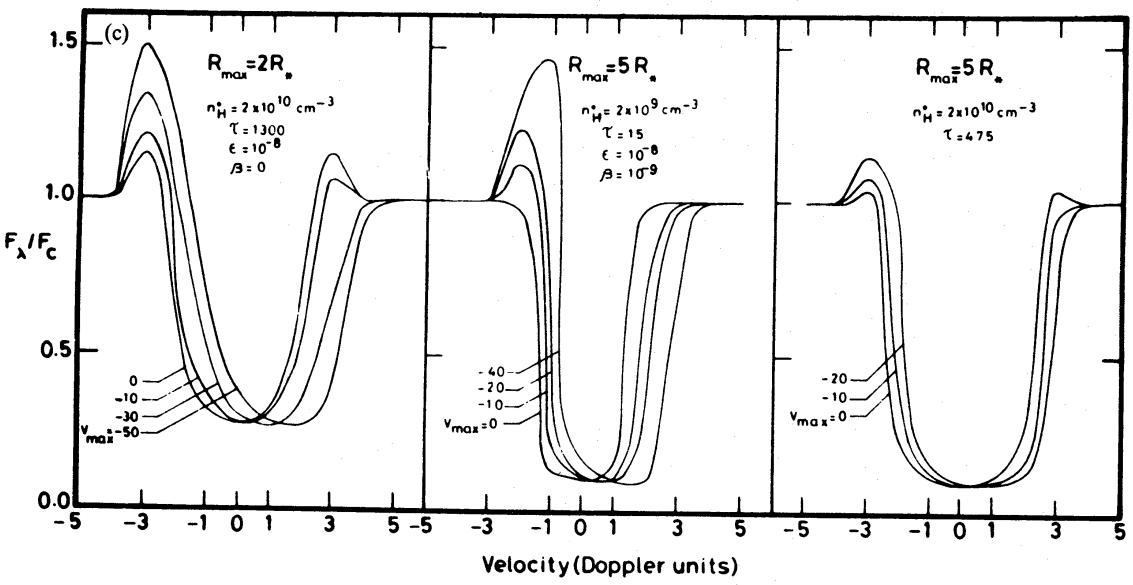

Figure 3–*continued*

large as 1000 (corresponding to $n_H^0=2\times10^{10}\,cm^{-3}$). Even though β was assumed to be zero, the computed equivalent widths (EQWs) of Hα absorption were never quite sufficient to match the observed values. For higher τs, the computing time becomes nearly prohibitive and τ larger than 1000 was not tried.

3.1.1.2 $R_{max}/R_*=5$. The profiles are not saturated in this case either, not even for very large densities like $n_H^0=10^{11}\,cm^{-3}$ ($\tau\sim4000$) unlike the isothermal case where for $\tau>500$, the cores were very flat which rendered the determination of blue displacements extremely difficult. The computed Hα strengths are sufficiently large; τ in the range 20–4000 covering the observed Hα EQWs. The initial densities for which good fits with the observed EQWs are obtained are consistently higher than in the isothermal calculations which may be understood as follows. In the varying temperature situation, in the shells close to R_*, n_2 is low in contrast to the large n_2 values for the 6000 K isothermal case. By the time n_2 reaches high values because of higher temperatures farther out, the total density has already considerably declined. n_2 does not attain high enough values to make up for the initial shortfall. In fact it also declines by a moderate amount (typically 20 per cent) due to ionization effects. Hence a higher initial density is needed in this case to obtain proper match with the observed EQWs. The behaviour of the blue and red emissions as a function of the velocity is similar to the previous case.

3.1.1.3 $R_{max}/R_*=8$. The cores are a bit saturated. The computed EQWs are high enough to match the observed Hα strengths. For the same n_H^0, τ here is lower than for $R_{max}=5R_*$ as can be seen in Fig. 2(a). By the time n_2 builds up, n_H has decreased much more than in the previous case because of its r^{-3} dependence. Therefore a higher n_H^0 is needed to obtain the same τ and match the observed EQWs. Since the same temperature range is spread over a larger region in this case, the ionization sets in a little closer to the inner boundary. This also contributes to the lower n_2. n_2 is consistently lower than in the previous case for a given n_H^0.

Like the other chromospheric extents, the emission appears on both the sides of the absorption for $V_{max}=0$, the peak value systematically increasing with τ. For $|V_{max}|\geq10\,km\,s^{-1}$, the blue emission disappears. The peak intensity of red emission increases for higher V_{max}.

3.1.2 Effect of $T_{II}(\tau)$

This choice of the temperature distribution is based on the schematic work of Dupree *et al.* (1984a, b) and Drake (1985). For $R_{max}=2R_*$, it is described by a climb from $T=T_*$ at R_*, linear in $\log r$, to $T=8000$ K at $1.2R_*$ and then a plateau till $1.5R_*$ followed by a slow rise to 8500 K till $2R_*$. For $R_{max}=5R_*$, it rises to 8000 K at $1.8R_*$ followed by a plateau till $3R_*$ and a further rise to 8500 K till R_{max}. The corresponding depth dependence of n_2 for two extents and for various choices of n_H^0 is shown in Fig. 2(b).

Due to rapid increase of temperature within the first few shells, the ionization effects appear close to the inner boundary (at $1.15R_*$ for $R_{max}=2R_*$) where the temperature is already close to 7000 K. Independent of n_H^0, for both the extents peak n_2 occurs at the 4th shell followed by a slow decline. The characteristics of the computed profiles are quite striking. Fig. 3(b) shows profiles for a specific set of parameters. The profiles are rather saturated at the core, particularly for $R_{max}=5R_*$. As expected, with increasing τ darker cores are obtained. The emission on either side of the absorption line is missing at $V_{max}=0$. It only appears when V_{max} is non-zero and on the red side, increasing with increasing V_{max}. It is not possible to produce blue emission at all with this temperature and density structure. In this sense, the atmosphere behaves like an isothermal one. The high temperatures prevailing over a large portion of the atmospheric extent contribute much higher thermal broadening than in the other cases, hence n_H^0s obtained to fit the observed EQWs are lower by more than an order of magnitude.

As in the previous case, the drop in n_H at any shell is more drastic for $R_{max}=5R_*$ than for $2R_*$. Therefore n_2 and the integrated τ turn out to be more for the latter for the same n_H^0. However, densities which fit the observed strengths are found to be roughly the same. A careful comparison of the Hα profiles for the two cases reveals that the profiles for $R_{max}=5R_*$ reach deeper and are more saturated for the same n_H^0, although τ is 1.5–2 times higher in the $R_{max}=2R_*$ case. Therefore, in spite of the different τs, the computed EQWs are roughly the same for the same n_H^0 in the two cases. Emission filling in the absorption giving an apparent effect of reduced absorption is strongly suspected for the $R_{max}=2R_*$ case. The source functions in this case decrease less rapidly (by a factor 50–100) over the region than in the case of the higher extent where they drop by a factor of nearly 500 (see Fig. 2b).

3.1.3 *Effect of* $T_{III}(\tau)$

Fig. 2(c) shows n_2 as a function of r. For $R_{max}=2R_*$, computations were carried out up to optical depths as large as $\tau=1300$ ($n_H^0=2\times10^{10}\,cm^{-3}$). A few profiles are displayed in Fig. 3(c). The profiles do not show any saturation and have a core-like quality. Emission is present on either side for $V_{max}=0$. As V_{max} increases, the absorption core shifts to the blue, partially covering up the blue emission and increasing the emission in the red. Blue emission vanishes at $V_{max}=-20\,km\,s^{-1}$ ($\sim 1V_{Dopp}$). The absorption strengths increase with τ. However, they fail to match the observed values even for $n_H^0=2\times10^{10}\,cm^{-3}$.

For $R_{max}=5R_*$, the computed profiles are slightly flattened at the core. The strength of absorption is large enough to match the observed EQWs for $n_H^0=2\times10^{10}\,cm^{-3}$ although this n_H^0 corresponds to $\tau=476$, much less than in the previous case. The source functions show a more rapid decline than in the $R_{max}=2R_*$ case as shown in Fig. 2(c). In the latter case, more emission filling within the absorption core cannot be ruled out. The emission lying on either side of the absorption wings is also higher in this case than for $R_{max}=5R_*$.

The overall higher temperature at every shell compared to $T_I(r)$ contributes larger thermal broadening. As a result, densities matching the observed EQWs are smaller in this case.

3.1.4 *Dependence of the line profiles on* ε *and* β

The shape and nature of the line profiles are very sensitive to β, the ratio of the continuum to line opacity. Fig. 4 shows the response to β for $T_I(r)$ and $T_{II}(r)$ with $R_{max}=5R_*$ for $V_{max}\sim-20\,km\,s^{-1}$. With a higher β, the line core is lifted more and red emission becomes progressively enhanced. $\beta=10^{-7}$ gives a strong wide emission (not shown in the figure). A higher ε produces a similar effect – lesser absorption and increased emission in the red. In both the cases, the higher value produces lower EQW of the absorption line and hence requires a higher n_H^0 to match the observed EQWs.

Although only the gross characteristics of the observed profiles have been used for comparison with the computed ones, it is also interesting to see how the profiles themselves match when superposed on one another. Fig. 5 shows observed profiles of two stars λ Vel and η Per along with the Hα profiles computed with three specific sets of parameters. As is evident from the figure, the line minimum of the absorption feature in these stars does not reach as deep as in the computed profiles and its red end is less steep. We note further that blue emission is absent in the computed profiles for this particular case. In η Per the observed red emission is displaced by a larger amount than could be satisfactorily reproduced by our solutions without disturbing the match of the line core displacement and the equivalent width.

The models constructed by us are able to reproduce line profiles with deep asymmetric absorption cores and bright emission in the red wing with non-zero velocities. The inadequacy of the present modelling lies in the absence of blue emission for outflow velocities larger than

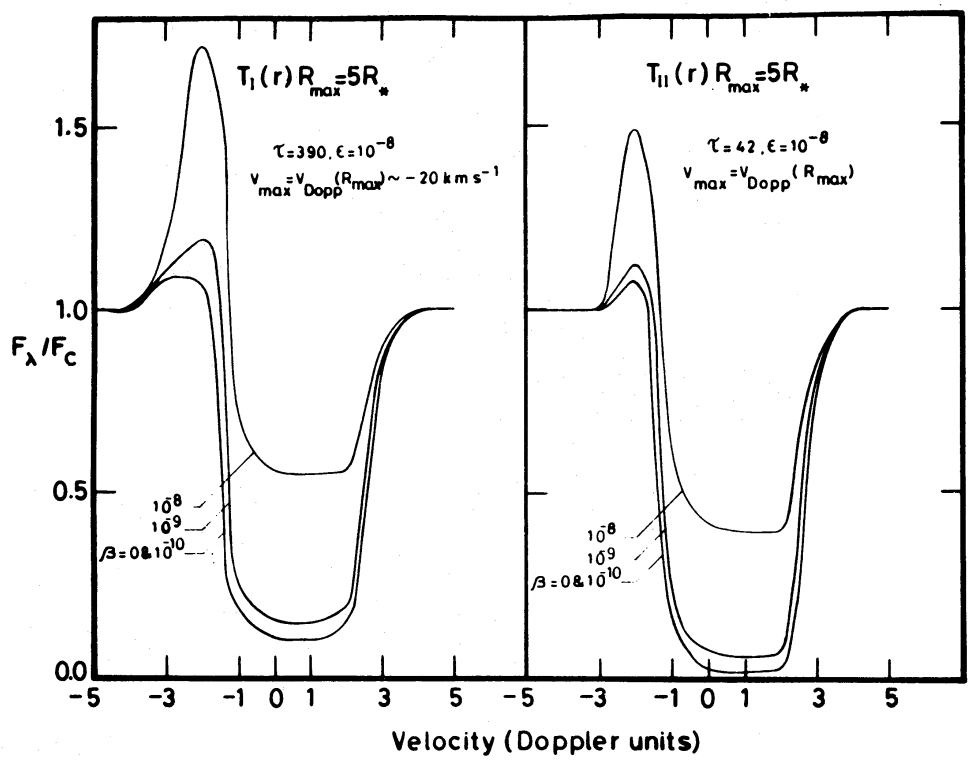

Figure 4. Response of the calculated Hα profiles to β for two temperature distributions $T_{\rm I}(r)$ and $T_{\rm II}(r)$. In both the cases $R_{\rm max}=5R_*$ and $V_{\rm max}=-20\,{\rm km\,s^{-1}}$.

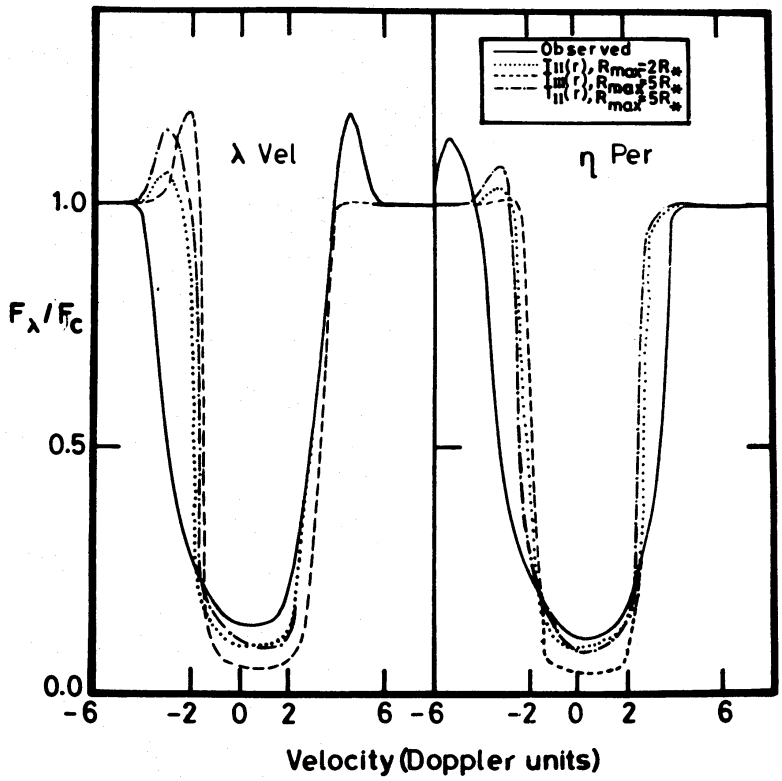

Figure 5. Comparison of observed profiles of λ Vel and η Per with Hα profiles calculated for three different sets of parameters as described in the inset.

$-10\,\mathrm{km\,s^{-1}}$. The observed line shifts are also on the same order. The present model assumes a simple wind with constant acceleration outward without any downflows. The chromospheres of supergiants under study are perhaps better represented by more complicated velocity patterns as emphasized by several authors (see Mihalas 1979; Linsky 1980). According to Reimers (1981) and later Dupree *et al.* (1984a, b), the origin of the blue and the red emission is not related to the mass outflow. Instead it can arise even in a static chromosphere with sufficient material at high enough temperature. They argue that Hα is optically thick. At the densities prevalent in the wind, Hα is photoelectrically controlled and appears in absorption with a blue asymmetry unless very optically thick. The deeper chromospheric layers thus give rise to emission. The earlier observations of Mallia & Pagel (1978) and Cacciari & Freeman (1983) have demonstrated that the blue emission peak is as often greater than the red as less. This is exactly analogous to the behaviour of the Ca II *H* and *K* in solar type stars (Linsky *et al.* 1979). If the blue emission peak is more intense than the red, it implies inflow of material that produces the overlying absorption.

3.2 TOTAL HYDROGEN DENSITIES, VELOCITY FIELDS AND MASS FLOW RATES

With important restrictions on the parameters, the calculations of the asymmetric chromospheric profiles can be used to estimate expansion velocities, densities and thus mass flow rates. For this purpose, we have limited ourselves to about seven sets from the extensive computer runs described above, each set referring to a specific choice of input parameters. The computations of line profiles in each set encompass a range of densities and expansion velocities. The equivalent width and the blueshift of the core were determined for each computed profile belonging to each set. The theoretical plots of EQW versus τ for each $V_{\max}$ and of line core displacement (LCD) versus $V_{\max}$ for each τ were obtained for each set. The exact procedure of determining the expansion velocity and the density from the fits with the observed is described in detail in Mallik (1982). Unique simultaneous solutions of n_{H}^0 and $V_{\max}$ were obtained for the 23 program stars in each case. Assuming a mass conservative flow in spherical symmetry, the rate of mass outflow was calculated in each case for the equation

$$\dot{M}=4\pi r^2\varrho(r)V(r)$$

which at $R_{\max}$ reduces to

$$\frac{\dot{M}}{M_\odot}\,(\mathrm{yr}^{-1})=4.47\times10^{-44}n_{\mathrm{H}}^0\left(\frac{R_*}{R_{\max}}\right)^3 V_{\max}R_{\max}^2$$

where n_{H}^0 is expressed in units of $\mathrm{cm^{-3}}$, $V_{\max}$ in $\mathrm{km\,s^{-1}}$ and $R_{\max}$ in cm.

The results are displayed in Table 1 for all the seven cases. The expansion velocities fall in the range $0.25V_{\mathrm{Dopp}}$ to about $2V_{\mathrm{Dopp}}$ and the densities at R_* (n_{H}^0) in the range 10^9–$10^{11}\,\mathrm{cm^{-3}}$. As anticipated and explained already, for $T_{\mathrm{I}}(r)$ and $T_{\mathrm{III}}(r)$ the initial densities (n_{H}^0) are higher than those for an isothermal chromosphere of 6000 K where no ionization effects were taken into account. For $R_{\max}=5R_*$, they are larger by a factor of 5–10 and for $R_{\max}=8R_*$ by a factor of 10–25. As described already they are higher for higher $R_{\max}$, being $10^{11}\,\mathrm{cm^{-3}}$ for $R_{\max}=8R_*$. The same is true of the optical depths. τ lies in the range 200–5000 – higher by more than one order of magnitude. The electron density n_{e} lies in the range 10^7–$10^9\,\mathrm{cm^{-3}}$. Brown & Carpenter (1984) had used the line flux ratios of the C II] 2325 Å multiplet and found for 11 K–M giants and supergiants that the e^- densities lie in the range $7.8<\log n_{\mathrm{e}}<8.3$. More recent work by Judge (1986a, b) based on new atomic data by Lennon *et al.* (1985) shows that Brown & Carpenter (1984) underestimated n_{e} by a factor of 3–5. Hence the expected n_{e} for early K supergiants is in the range $10^{8.3}$–$10^{8.8}$. Our matching electron densities are very similar. Table 2(a) and (b) list the run of

Table 1. Chromospheric densities, expansion velocities and mass outflow rates.

Star	$T_I(r)$: $\epsilon = 10^{-8}$, $\beta = 10^{-9}$, $R_{max} = 5R_*$			$T_I(r)$: $\epsilon = 10^{-8}$, $\beta = 0$, $R_{max} = 5R_*$			$T_I(r)$: $\epsilon = 10^{-8}$, $\beta = 10^{-9}$, $R_{max} = 8R_*$			$T_{II}(r)$: $\epsilon = 10^{-8}$, $\beta = 10^{-9}$, $R_{max} = 2R_*$			$T_{II}(r)$: $\epsilon = 10^{-8}$, $\beta = 10^{-8}$, $R_{max} = 2R_*$			$T_{II}(r)$: $\epsilon = 10^{-8}$, $\beta = 10^{-9}$, $R_{max} = 5R_*$			$T_{III}(r)$: $\epsilon = 10^{-8}$, $\beta = 10^{-9}$, $R_{max} = 5R_*$		
	$n_H^\circ(+10)$ cm^{-3}	V_{max} $kmsec^{-1}$	$\dot{M}/M_\odot(-7)$ yr^{-1}	$n_H^\circ(+10)$ cm^{-3}	V_{max} $kmsec^{-1}$	$\dot{M}/M_\odot(-7)$ yr^{-1}	$n_H^\circ(+11)$ cm^{-3}	V_{max} $kmsec^{-1}$	$\dot{M}/M_\odot(-7)$	$n_H^\circ(+9)$ cm^{-3}	V_{max} $kmsec^{-1}$	$\dot{M}/M_\odot(-8)$ yr^{-1}	$n_H^\circ(+9)$ cm^{-3}	V_{max} $kmsec^{-1}$	$\dot{M}/M_\odot(-8)$ yr^{-1}	$n_H^\circ(+9)$ cm^{-3}	V_{max} $kmsec^{-1}$	$\dot{M}/M_\odot(-8)$ yr^{-1}	$n_H^\circ(+10)$ cm^{-3}	V_{max} $kmsec^{-1}$	$\dot{M}/M_\odot(-7)$ yr^{-1}
ϵ Gem	7.2	10.8	7.0	5.2	13.0	6.0	1.4	8.7	6.6	4.7	9.3	9.8	6.2	9.6	13.3	4.7	8.7	3.6	2.3	11.0	2.3
HD 77912	1.0	20.2	1.8	1.0	23.0	2.1	-	-	-	1.0	22.5	5.0	1.7	20.3	7.7	1.1	17.0	1.7	0.5	19.5	0.9
33 Sgr	5.4	6.4	3.1	2.4	8.6	1.8	1.2	5.7	3.7	4.3	6.1	5.9	4.7	6.0	6.3	3.3	5.6	1.6	1.5	7.0	0.9
ζ Cep	8.6	19.5	15.0	6.2	22.5	12.5	1.6	14.7	13.1	5.3	20.5	24.3	6.4	16.8	24.0	5.2	14.7	6.8	3.2	20.0	5.7
HD 196093	-	-	-	0.8	30.7	2.2	-	-	-	1.0	31.7	7.1	1.0	31.0	6.9	1.1	24.0	2.4	0.3	30.0	0.8
ϵ Peg	8.2	11.7	8.6	6.4	14.3	8.2	2.0	9.2	10.3	5.3	10.5	12.4	6.9	10.5	16.1	5.0	9.3	4.2	3.1	12.0	3.3
η Per	10.0	10.0	8.9	10.0	12.2	10.9	2.0	8.3	9.3	5.9	8.7	11.4	7.6	9.0	15.3	5.7	8.0	4.0	4.7	10.5	4.4
HD 17958	-	-	-	0.8	31.0	2.2	-	-	-	1.0	30.0	6.7	1.0	28.3	6.3	1.1	22.2	2.2	0.2	28.0	0.5
o'CMa	0.8	9.6	0.7	0.8	13.6	1.0	-	-	-	1.0	9.3	2.1	-	-	-	1.0	8.0	0.7	0.2	11.6	0.2
41 Gem	1.2	13.6	1.5	1.0	16.7	1.5	0.2	9.7	1.3	1.7	12.3	4.7	1.7	13.0	4.9	1.1	11.2	1.1	0.5	13.0	0.6
HD 56577	2.0	8.8	1.6	1.2	10.7	1.2	0.5	6.7	1.9	1.8	7.8	3.1	2.0	8.0	3.6	2.0	7.0	0.9	0.8	8.4	0.6
HD 62576	0.8	23.0	1.6	0.8	30.3	2.2	-	-	-	1.0	28.0	6.3	-	-	-	1.0	19.7	1.8	0.2	25.0	0.5
HD 68553	-	-	-	0.8	43.7	3.1	-	-	-	1.6	30.0	10.7	1.3	37.0	10.8	1.2	39.7	4.3	0.5	40.0	1.9
HD 80108	-	-	-	2.0	34.3	6.1	0.8	22.0	10.2	1.7	34.3	13.0	3.7	27.0	22.3	2.7	25.7	6.1	1.2	33.0	3.5
HD 91056	-	-	-	26.2	13.0	30.4	2.1	9.2	10.8	8.9	10.5	20.8	12.0	9.6	25.7	7.8	8.3	5.8	9.6	12.0	10.2
β Arae	-	-	-	1.6	30.3	4.3	0.6	18.3	6.5	1.5	30.9	10.4	2.6	26.0	15.1	2.0	21.7	3.9	0.9	28.0	2.3
HD 4817	9.6	17.0	14.6	6.2	20.3	11.3	2.2	12.0	13.4	5.3	17.0	20.1	6.7	14.6	21.9	5.1	12.7	5.8	3.4	17.0	5.3
λ Vel	5.0	17.4	7.8	3.2	20.0	5.7	1.1	12.0	7.4	3.3	16.0	11.8	4.3	15.0	14.4	3.1	13.1	3.6	1.8	17.0	2.7
HD 89388	-	-	-	2.8	36.0	9.0	1.1	22.3	14.0	3.5	34.5	26.6	4.8	28.8	30.9	3.7	25.9	8.6	1.8	33.0	5.3
HD 137709	6.0	13.2	7.1	3.2	15.9	4.5	1.2	10.0	6.5	3.9	11.3	9.8	4.8	11.5	12.3	3.4	10.3	3.2	1.6	13.0	1.9
ξ Cyg	-	-	-	20.0	15.0	26.8	1.9	10.0	10.6	7.7	11.3	19.4	9.9	10.8	23.9	7.0	9.8	6.1	8.0	13.0	9.3
σ CMa	8.0	15.4	11.1	4.2	18.2	6.8	1.4	11.0	8.9	4.1	13.8	12.6	5.3	13.0	15.4	3.9	11.2	3.9	2.1	15.0	2.8
HD 216946	-	-	-	5.0	28.3	12.7	1.3	17.3	12.2	4.8	27.0	29.0	6.7	20.6	30.8	4.3	19.0	7.3	2.9	25.0	6.4

Table 2.

$r(10^{13}$ cn)	T(°K)	n_e(cm^{-3})	n_H(cm^{-3})	n_2(cm^{-3})	$\tau_{H\alpha}$	V_{flow}(km s^{-1})
(a) Model for ε Gem with $T_{II}(r)$ and $R_{max}=2\,R_*$.						
2.0	8.5(3)	6.5(9)	7.1(8)	8.5(1)	1.4(1)	9.3
1.95	8.45(3)	7.0(9)	7.5(8)	8.6(1)	2.8(1)	8.8
1.9	8.4(3)	7.6(9)	7.9(8)	8.8(1)	4.3(1)	8.35
1.85	8.35(3)	8.2(9)	8.4(8)	9.0(1)	5.8(1)	7.9
1.8	8.28(3)	9.0(9)	9.0(8)	8.8(1)	7.3(1)	7.45
1.75	8.23(3)	9.8(9)	9.6(8)	9.0(1)	8.8(1)	7.0
1.7	8.18(3)	1.1(10)	1.0(9)	9.3(1)	1.0(2)	6.5
1.65	8.13(3)	1.2(10)	1.1(9)	9.5(1)	1.2(2)	6.05
1.6	8.05(3)	1.3(10)	1.2(9)	9.4(1)	1.4(2)	5.6
1.55	8.0(3)	1.4(10)	1.3(9)	9.6(1)	1.5(2)	5.1
1.5	8.0(3)	1.6(10)	1.4(9)	1.1(2)	1.7(2)	4.65
1.45	8.0(3)	1.7(10)	1.5(9)	1.2(2)	1.9(2)	4.2
1.4	8.0(3)	1.9(10)	1.6(9)	1.4(2)	2.1(2)	3.75
1.35	8.0(3)	2.2(10)	1.8(9)	1.6(2)	2.4(2)	3.25
1.3	8.0(3)	2.4(10)	2.0(9)	1.8(2)	2.7(2)	2.8
1.25	8.0(3)	2.8(10)	2.2(9)	2.1(2)	3.1(2)	2.3
1.2	6.85(3)	1.5(10)	2.5(9)	2.2(2)	3.4(2)	1.85
1.15	5.7(3)	1.5(10)	2.9(9)	1.4(1)	3.5(2)	1.4
1.1	4.55(3)	1.2(8)	3.5(9)	8.6(−2)	3.5(2)	0.95
1.05	3.4(3)	1.8(6)	5.0(9)	1.5(−5)	3.5(2)	0.5
(b) Model for λ Vel with $T_{III}(r)$ and $R_{max}=5\,R_*$.						
5.0	8.0(3)	1.7(8)	4.4(8)	1.6(1)	1.1(1)	17.0
4.8	8.0(3)	1.9(8)	4.8(8)	1.9(1)	2.4(1)	16.2
4.6	8.0(3)	2.2(8)	5.2(8)	2.3(1)	3.9(1)	15.3
4.4	8.0(3)	2.5(8)	5.8(8)	2.7(1)	5.7(1)	14.4
4.2	8.0(3)	2.9(8)	6.4(8)	3.3(1)	7.9(1)	13.6
4.0	8.0(3)	3.4(8)	7.0(8)	4.0(1)	1.1(2)	12.8
3.8	7.8(3)	3.8(8)	7.9(8)	5.3(1)	1.4)2)	11.9
3.6	7.6(3)	4.1(8)	8.8(8)	6.9(1)	1.9(2)	11.0
3.4	7.4(3)	4.2(8)	1.0(9)	8.4(1)	2.4(2)	10.2
3.2	7.2(3)	4.1(8)	1.1(9)	9.1(1)	3.0(2)	9.4
3.0	7.0(3)	3.7(8)	1.3(9)	8.7(1)	3.6(2)	8.5
2.8	6.7(3)	2.9(8)	1.5(9)	7.2(1)	4.1(2)	7.7
2.6	6.4)3)	1.9(8)	1.8(9);	4.7(1)	4.4(2)	6.8
2.4	6.1(3)	1.0(8)	2.2(9)	2.6(1)	4.6)2)	5.9
2.2	5.8(3)	6.6(7)	2.7(9)	1.2)1)	4.7(2)	5.2
2.0	5.4(3)	4.2(7)	3.4(9)	4.1	4.7(2)	4.3
1.8	5.0(3)	2.5(7)	4.4(9)	1.1	4.7(2)	3.4
1.6	4.6(3)	1.0(7)	6.0(9)	1.5(−1)	4.7(2)	2.5
1.4	4.0(3)	2.8(6)	9.0(9)	7.8(−3)	4.7(2)	1.7
1.2	3.4(3)	3.5(5)	2.0(10)	6.0(−5)	4.7(2)	0.9

atmospheric parameters with distance above the photosphere for ε Gem and λ Vel respectively for a typical model for each.

The mass loss rates are larger by a factor of approximately 7 than the isothermal values (see Mallik 1987) which lie in the range 3×10^{-7} to $1.2\times10^{-8}\,M_\odot\,yr^{-1}$ for $R_{max}=6R_*$. For $T_{III}(r)$ the n_H^0s, τ and $\dot{M}/M_\odot$ are lower than for $T_I(r)$ but they are still higher than the isothermal values. However, for $T_{II}(r)$ the rates of mass flow lie in the range 7×10^{-9} to $9\times10^{-8}\,M_\odot\,yr^{-1}$, lower than the isothermal rates by a factor of 2–3 for $5R_*$ and 2–10 for $2R_*$. The densities and the optical

depths are also lower, matching densities being on the order $10^9\,\mathrm{cm}^{-3}$. This particular temperature structure contributes larger thermal broadening to Hα widths, hence lower n_{H}^0 and $\dot{M}/M_\odot$ are inferred.

It is important to emphasize once again that the above analysis allows several combinations of input parameters to yield solutions that would fit an observed profile. This non-uniqueness of the solution renders the calculations of rates of mass outflow non-definitive. The sensitivity of the mass outflow to several model dependent parameters has been elaborated by Goldberg (1979), Castor (1981), Trimble (1984) and Mallik (1986). Nevertheless, the above analysis gives us an idea of total hydrogen densities, electron and $n=2$ densities and outflow velocities. For matter to be actually lost from a star, it has to exceed the escape velocity which for a cool supergiant star is typically $110\,\mathrm{km\,s}^{-1}$ at its surface. For extended atmospheres where $R_{\max}$ is several times the stellar radius, the velocity required for escape is much less as it decreases as $r^{1/2}$. Such lower velocities have been observed in supergiant stars. Even if the velocity is not large enough for material to escape, the velocity gradients determined above indicate the velocities with which the chromosphere expands, while the matter is still gravitationally bound to the star.

4 Conclusions

Computations of the Hα line profiles have been performed in a non-LTE moving chromosphere with a temperature rise to simulate the observed Hα characteristics in G and K supergiants. The comoving frame radiative transfer code has been modified to incorporate explicitly the effects of hydrogen ionization. A source function appropriate for a two-level atom with continuum has been used. The sensitivity of the Hα profiles to a wide variety of temperature structures, velocity gradients chromospheric extents and densities has been explored and illustrated. The salient features of this analysis are the following.

(i) The consequences of inclusion of temperature gradient and ionization are:

(a) The profiles are more rounded and less saturated (than those in isothermal calculations); more for a linear $T(r)$ than for a $T(r)$ with a steep climb and wide plateau.

(b) The Hα optical depths are consistently much higher than the isothermal values in the case of the linear $T(r)$ and $T(r)$ with a plateau only in the outermost layers. For $T(r)$ with a steep climb and a wide plateau, they are lower.

(c) Symmetric red and blue emissions flank the absorption for $V_{\max}=0$ for the first and the third temperature distributions. With increasing $V_{\max}$, the absorption core shifts to the blue reducing thereby the blue emission while enhancing the red emission until $V_{\max}\simeq V_{\mathrm{Dopp}}$ when blue emission is effaced and red emission is even brighter. On the other hand for the second T distribution, they are absent for $V_{\max}=0$. For a non-zero $V_{\max}$, red emission appears and increases with increasing $V_{\max}$.

(ii) Higher n_{H}^0 (and hence $\tau_{\mathrm{H}\alpha}$) yields stronger absorption.

(iii) A higher continuum to line opacity ratio β and/or collision parameter ε gives less deep absorption and enhanced emission peak in the red.

Best fits with the observed profiles yield densities at $R_{\max}$ in the range 10^9–$10^{11}\,\mathrm{cm}^{-3}$ and the consequent integrated optical depths in the range 50–5000. The outflow velocities vary from 0.25 to 2 times the Doppler velocity (thermal+microturbulent). For the range of parameters considered, the rates of mass outflow from the chromospheres of the stars studied lie in the range 10^{-7} to $10^{-9}\,M_\odot\,\mathrm{yr}^{-1}$. The mass flow rate depends quite crucially on the choice of the input parameters. Although the choice of most of the parameters is based on information already known about the chromospheres of these stars, the above determination gives an order of magnitude estimate. It is extremely important to understand how the Hα line forms in cool

chromospheres. A two-level atom with continuum is not an adequate description of its formation. Being a non-resonance line, its proper treatment must explicitly consider the equation of statistical equilibrium for multilevel configurations. Also, as has been stressed earlier, an appropriate self-consistent temperature distribution emerges only by treating the energy equation properly in the stellar wind theory similar to the semi-empirical approach of Hartmann & MacGregor (1980) and Hartmann & Avrett (1984). The origin of the red and the blue emissions can only be studied properly after accounting for all this into the model.

It is impossible to extract information on the physical properties of the chromosphere uniquely from one observed line profile. One would greatly benefit from future observations and similar analysis as described above of different lines formed in different regions of the chromosphere. Judge (1987, 1988) has described several important chromospheric diagnostics ranging from ultraviolet in particular to the infrared and radio regions. Carpenter (1984) has deduced, e.g., the depth variation of velocity flows in α Ori by studying Fe II lines of different opacities. Among the more easily accessible, ground-based diagnostics are the Na I *D* lines at $\lambda\lambda$5890, 5896 and the K I lines at $\lambda\lambda$7665, 7699. These species are easily ionized and the lines form only in the outermost layers where the outflow reaches a terminal velocity. Apart from being sensitive to the degree of ionization in the wind, they in conjunction with Hα which forms in the inner accelerating region of the chromosphere give a hold on velocity gradients.

It is worth exploring if the blue and the red emission flanking the Hα absorption is time-variable in strength and/or Doppler shift. A detailed study of the variability might give a clue to the origin and the nature of the flow.

Acknowledgments

We are indebted to Professor A. Peraiah for allowing us to use his comoving frame code of radiative transfer. It is a pleasure to acknowledge several fruitful discussions with K. E. Rangarajan and D. Mohan Rao and we thank them for their ever ready and untiring help during the computations. Finally we would like to thank the referee for the many useful comments which have helped to improve the quality of the paper a great deal.

References

Ayres, T. R. & Linsky, J. L., 1975. *Astrophys. J.*, **200,** 660.
Ayres, T. R., Linsky, J. L., Basri, G. S., Landsman, W., Henry, R. C., Mous, H. W. & Stencel, R. E., 1982. *Astrophys. J.*, **256,** 500.
Baliunas, S. L., Avrett, E. H., Hartmann, L. & Dupree, A. K., 1979. *Astrophys. J.*, **233,** L129.
Basri, G. S., Linsky, J. L. & Ericksson, K., 1981. *Astrophys. J.*, **251,** 162.
Boesgaard, A. M. & Hagen, W., 1979. *Astrophys. J.*, **231,** 128.
Brown, A. & Carpenter, K. G., 1984. *Astrophys. J.*, **287,** L43.
Cacciari, C. & Freeman, K. C., 1983. *Astrophys. J.*, **268,** 185.
Carpenter, K. G., 1984. *Astrophys. J.*, **285,** 181.
Castor, J. I., 1981. In: *Physical Processes in Red Giants*, p. 285, eds Iben, I., Jr. & Renzini, A., Reidel, Dordrecht, Holland.
Cram, L. E. & Mullan, D. J., 1985. *Astrophys. J.*, **294,** 626.
Drake, S. A., 1985. In: *Progress in Stellar Spectral Line Formation Theory*, p. 351, eds Beckman, J. E. & Crivellari, L., Reidel, Dordrecht, Holland.
Drake, S. A. & Linsky, J. L., 1983. *Astrophys. J.*, **274,** L77.
Drake, S. A. & Linsky, J. L., 1986. *Astr. J.*, **91,** 602.
Dupree, A. K., 1986. *Ann. Rev. Astr. Astrophys.*, **24,** 377.
Dupree, A. K., Hartmann, L. & Avrett, E. H., 1984a. *Astrophys. J.*, **281,** L37.
Dupree, A. K., Avrett, E. H., Hartmann, L. & Smith, G., 1984b. In: *Proc. 4th European IUE Conference,* Rome, p. 191, RSA SP-218.
Gebbie, K. B. & Steinitz, R., 1974. *Astrophys. J.*, **188,** 399.

Goldberg, L., 1979. *Q. Jl R. astr. Soc.*, **20,** 361.
Goldberg, L. *et al.*, 1982. In: *Second Cambridge Workshop on Cool Stars, Stellar Systems and the Sun,* p. 131, eds Giampapa, M. S. & Golub, L., *SAO Special Report 392.*
Hartmann, L., 1983. In: *Highlights of Astronomy,* p. 549, Vol. 6, ed. West, R. M., Reidel, Dordrecht, Holland.
Hartmann, L. & Avrett, E. H., 1984. *Astrophys. J.*, **284,** 238.
Hartmann, L. & MacGregor, K. B., 1980. *Astrophys. J.*, **242,** 260.
Hartmann, L., Dupree, A. K. & Raymond, J. C., 1981. *Astrophys. J.*, **246,** 193.
Hebden, J. C., Eckart, A. & Hege, E. K., 1987. *Astrophys. J.*, **314,** 690.
Hummer, D. S. & Rybicki, G., 1968. *Astrophys. J.*, **153,** L107.
Jordan, C. & Linsky, J. L., 1987. In: *Exploring the Universe with the IUE Satellite,* p. 259, Reidel, Dordrecht, Holland.
Judge, P. G., 1986a. *Mon. Not. R. astr. Soc.*, **221,** 119.
Judge, P. G., 1986b. *Mon. Not. R. astr. Soc.*, **223,** 239.
Judge, P. G., 1987. In: *Fifth Cambridge Workshop on Cool Stars, Stellar Systems and the Sun,* eds Stencel, R. E. & Linsky, J. L., Springer-Verlag, Berlin.
Judge, P. G., 1988. *Mon. Not. R. astr. Soc.*, **231,** 419.
Keltch, W., Linsky, J. L. & Worden, S., 1979. *Astrophys. J.*, **229,** 700.
Kuhi, L. V., 1974. In: *Highlights of Astronomy,* Vol. 3, p. 121, ed. Contopoulos, G., Reidel, Dordrecht, Holland.
Lennon, D. J., Dufton, P. L., Hibbert, A. & Kingston, A. E., 1985. *Astrophys. J.*, **294,** 200.
Linsky, J. L., 1980. *Ann. Rev. Astr. Astrophys.*, **18,** 439.
Linsky, J. L., 1985. In: *Mass Loss from Red Giants,* p. 31, eds Morris, M. & Zuckerman, B., Reidel, Dordrecht, Holland.
Linsky, J. L., Worden, S. P., McClintock, W. & Robertson, R. M., 1979. *Astrophys. J. Suppl.*, **41,** 47.
Mallia, E. A. & Pagel, B. E. J., 1978. *Mon. Not. R. astr. Soc.*, **184,** 55.
Mallik, S. V., 1979. *PhD thesis,* Madurai Kamaraj University, Madurai.
Mallik, S. V., 1982. *J. Astrophys. Astr.*, **3,** 39.
Mallik, S. V., 1986. *Mon. Not. R. astr. Soc.*, **222,** 307.
Mallik, S. V., 1987. *Mon. Not. R. astr. Soc.*, **227,** 543 (Erratum).
Mihalas, D., 1979. *Mon. Not. R. astr. Soc.*, **189,** 671.
Mihalas, D., Kunasz, P. B. & Hummer, D. G., 1975. *Astrophys. J.*, **202,** 465.
Mihalas, D., Shine, R. A., Kunasz, P. B. & Hummer, D. G., 1976. *Astrophys. J.*, **205,** 492.
Peraiah, A., 1980a. *Acta. Astr.* **30,** 525.
Peraiah, A., 1980b. *J. Astrophys. Astr.*, **1,** 101.
Peraiah, A., 1981. *Astrophys. Space Sci.*, **77,** 243.
Reimers, D., 1981. In: *Physical Processes in Red Giants,* p. 269, eds Iben, I., Jr & Renzini, A., Reidel, Dordrecht, Holland.
Trimble, V., 1984. *Comm. Astrophys.*, **10,** 167.
Vernazza, J. E., Avrett, E. H. & Loeser, R., 1973. *Astrophys. J.*, **184,** 605.
Zarro, D. M., 1984. *Astrophys. J.*, **285,** 232.
Zarro, D. M. & Rodgers, A. W., 1983. *Astrophys. J. Suppl.*, **53,** 815.